

Non-contact single shot elastography using line field low coherence holography

CHIH-HAO LIU,¹ ALEXANDER SCHILL,¹ CHEN WU,¹ MANMOHAN SINGH,¹
AND KIRILL V. LARIN^{1,2,3,*}

¹Department of Biomedical Engineering, University of Houston, 3605 Cullen Boulevard, Houston, Texas 77204, USA

²Interdisciplinary Laboratory of Biophotonics, Tomsk State University, Tomsk, Russia

³Molecular Physiology and Biophysics, Baylor College of Medicine, One Baylor Plaza, Houston, Texas 77584, USA

*klarin@uh.edu

Abstract: Optical elastic wave imaging is a powerful technique that can quantify local biomechanical properties of tissues. However, typically long acquisition times make this technique unfeasible for clinical use. Here, we demonstrate non-contact single shot elastographic holography using a line-field interferometer integrated with an air-pulse delivery system. The propagation of the air-pulse induced elastic wave was imaged in real time, and required a single excitation for a line-scan measurement. Results on tissue-mimicking phantoms and chicken breast muscle demonstrated the feasibility of this technique for accurate assessment of tissue biomechanical properties with an acquisition time of a few milliseconds using parallel acquisition.

© 2016 Optical Society of America

OCIS codes: (110.4500) Optical coherence tomography; (170.0110) Imaging systems; (170.0170) Medical optics and biotechnology.

References and links

1. J. F. Greenleaf, M. Fatemi, and M. Insana, "Selected methods for imaging elastic properties of biological tissues," *Annu. Rev. Biomed. Eng.* **5**(1), 57–78 (2003).
2. J. L. Gennisson, T. Deffieux, M. Fink, and M. Tanter, "Ultrasound elastography: principles and techniques," *Diagn. Interv. Imaging* **94**(5), 487–495 (2013).
3. A. Manduca, T. E. Oliphant, M. A. Dresner, J. L. Mahowald, S. A. Kruse, E. Amromin, J. P. Felmlee, J. F. Greenleaf, and R. L. Ehman, "Magnetic resonance elastography: non-invasive mapping of tissue elasticity," *Med. Image Anal.* **5**(4), 237–254 (2001).
4. S. Wang and K. V. Larin, "Shear wave imaging optical coherence tomography (SWI-OCT) for ocular tissue biomechanics," *Opt. Lett.* **39**(1), 41–44 (2014).
5. D. Huang, E. A. Swanson, C. P. Lin, J. S. Schuman, W. G. Stinson, W. Chang, M. R. Hee, T. Flotte, K. Gregory, C. A. Puliafito, and J. G. Fujimoto, "Optical coherence tomography," *Science* **254**(5035), 1178–1181 (1991).
6. J. Schmitt, "OCT elastography: imaging microscopic deformation and strain of tissue," *Opt. Express* **3**(6), 199–211 (1998).
7. S. Wang and K. V. Larin, "Optical coherence elastography for tissue characterization: a review," *J. Biophotonics* **8**(4), 279–302 (2015).
8. M. Singh, J. Li, S. Vantipalli, S. Wang, Z. Han, A. Nair, S. R. Aglyamov, M. D. Twa, and K. V. Larin, "Noncontact elastic wave imaging optical coherence elastography for evaluating changes in corneal elasticity due to crosslinking," *IEEE J. Sel. Top. Quantum Electron.* **22**, 1–11 (2016).
9. C. H. Liu, Y. Du, M. Singh, C. Wu, Z. Han, J. Li, A. Chang, C. Mohan, and K. V. Larin, "Classifying murine glomerulonephritis using optical coherence tomography and optical coherence elastography," *J. Biophotonics* (2016).
10. S. Wang, A. L. Lopez 3rd, Y. Morikawa, G. Tao, J. Li, I. V. Larina, J. F. Martin, and K. V. Larin, "Noncontact quantitative biomechanical characterization of cardiac muscle using shear wave imaging optical coherence tomography," *Biomed. Opt. Express* **5**(7), 1980–1992 (2014).
11. S. Wang and K. V. Larin, "Noncontact depth-resolved micro-scale optical coherence elastography of the cornea," *Biomed. Opt. Express* **5**(11), 3807–3821 (2014).
12. M. Singh, C. Wu, C. H. Liu, J. Li, A. Schill, A. Nair, and K. V. Larin, "Phase-sensitive optical coherence elastography at 1.5 million A-Lines per second," *Opt. Lett.* **40**(11), 2588–2591 (2015).
13. A. Nahas, M. Tanter, T. M. Nguyen, J. M. Chassot, M. Fink, and A. Claude Boccara, "From supersonic shear wave imaging to full-field optical coherence shear wave elastography," *J. Biomed. Opt.* **18**(12), 121514 (2013).

14. Y. Nakamura, S. Makita, M. Yamanari, M. Itoh, T. Yatagai, and Y. Yasuno, "High-speed three-dimensional human retinal imaging by line-field spectral domain optical coherence tomography," *Opt. Express* **15**(12), 7103–7116 (2007).
15. D. J. Fechtig, B. Grajciar, T. Schmoll, C. Blatter, R. M. Werkmeister, W. Drexler, and R. A. Leitgeb, "Line-field parallel swept source MHz OCT for structural and functional retinal imaging," *Biomed. Opt. Express* **6**(3), 716–735 (2015).
16. M. K. Kim, "Principles and techniques of digital holographic microscopy," *J. Photonics Energy* **1**, 018005 (2010).
17. S. Li, K. D. Mohan, W. W. Sanders, and A. L. Oldenburg, "Toward soft-tissue elastography using digital holography to monitor surface acoustic waves," *J. Biomed. Opt.* **16**(11), 116005 (2011).
18. K. D. Mohan and A. L. Oldenburg, "Elastography of soft materials and tissues by holographic imaging of surface acoustic waves," *Opt. Express* **20**(17), 18887–18897 (2012).
19. Z. Han, J. Li, M. Singh, C. Wu, C. H. Liu, S. Wang, R. Idugboe, R. Raghunathan, N. Sudheendran, S. R. Aglyamov, M. D. Twa, and K. V. Larin, "Quantitative methods for reconstructing tissue biomechanical properties in optical coherence elastography: a comparison study," *Phys. Med. Biol.* **60**(9), 3531–3547 (2015).
20. J. Li, Z. Han, M. Singh, M. D. Twa, and K. V. Larin, "Differentiating untreated and cross-linked porcine corneas of the same measured stiffness with optical coherence elastography," *J. Biomed. Opt.* **19**(11), 110502 (2014).
21. P. Massatsch, F. Charrière, E. Cuhe, P. Marquet, and C. D. Depeursinge, "Time-domain optical coherence tomography with digital holographic microscopy," *Appl. Opt.* **44**(10), 1806–1812 (2005).
22. K. Creath, "Phase-shifting speckle interferometry," *Appl. Opt.* **24**(18), 3053 (1985).
23. S. Wang, K. V. Larin, J. S. Li, S. Vantipalli, R. K. Manapuram, S. Aglyamov, S. Emelianov, and M. D. Twa, "A focused air-pulse system for optical-coherence-tomography-based measurements of tissue elasticity," *Laser Phys. Lett.* **10**(7), 075605 (2013).
24. B. Qiang, J. Greenleaf, M. Oyen, and X. Zhang, "Estimating material elasticity by spherical indentation load-relaxation tests on viscoelastic samples of finite thickness," *IEEE Trans. Ultrason. Ferroelectr. Freq. Control* **58**(7), 1418–1429 (2011).
25. L. R. Correia, G. S. Mittal, and O. A. Basir, "Ultrasonic detection of bone fragment in mechanically deboned chicken breasts," *Innov. Food Sci. Emerg.* **9**(1), 109–115 (2008).
26. M. M. Nguyen, S. Zhou, J. L. Robert, V. Shamdassani, and H. Xie, "Development of oil-in-gelatin phantoms for viscoelasticity measurement in ultrasound shear wave elastography," *Ultrasound Med. Biol.* **40**(1), 168–176 (2014).
27. J. Meneses, T. Gharbi, and P. Humbert, "Phase-unwrapping algorithm for images with high noise content based on a local histogram," *Appl. Opt.* **44**(7), 1207–1215 (2005).
28. M. Pernot, K. Fujikura, S. D. Fung-Kee-Fung, and E. E. Konofagou, "ECG-gated, mechanical and electromechanical wave imaging of cardiovascular tissues in vivo," *Ultrasound Med. Biol.* **33**(7), 1075–1085 (2007).
29. P. Song, X. Bi, D. C. Mellema, A. Manduca, M. W. Urban, P. A. Pellikka, S. Chen, and J. F. Greenleaf, "Pediatric cardiac shear wave elastography for quantitative assessment of myocardial stiffness: a pilot study in healthy controls," *Ultrasound Med. Biol.* **42**(8), 1719–1729 (2016).
30. J. L. Gennisson, T. Deffieux, E. Macé, G. Montaldo, M. Fink, and M. Tanter, "Viscoelastic and anisotropic mechanical properties of in vivo muscle tissue assessed by supersonic shear imaging," *Ultrasound Med. Biol.* **36**(5), 789–801 (2010).
31. H. C. Wang, S. Fleming, Y. C. Lee, S. Law, M. Swain, and J. Xue, "Laser ultrasonic surface wave dispersion technique for non-destructive evaluation of human dental enamel," *Opt. Express* **17**(18), 15592–15607 (2009).
32. C. Ai and J. C. Wyant, "Effect of piezoelectric transducer nonlinearity on phase shift interferometry," *Appl. Opt.* **26**(6), 1112–1116 (1987).
33. L. Huang, Q. Kemao, B. Pan, and A. K. Asundi, "Comparison of Fourier transform, windowed Fourier transform, and wavelet transform methods for phase extraction from a single fringe pattern in fringe projection profilometry," *Opt. Lasers Eng.* **48**(2), 141–148 (2010).
34. J. Burke and H. Helmers, "Spatial versus temporal phase shifting in electronic speckle-pattern interferometry: noise comparison in phase maps," *Appl. Opt.* **39**(25), 4598–4606 (2000).
35. F. C. Delori, R. H. Webb, and D. H. Sliney, "Maximum permissible exposures for ocular safety (ANSI 2000), with emphasis on ophthalmic devices," *J. Opt. Soc. Am. A* **24**(5), 1250–1265 (2007).

1. Introduction

Altered tissue mechanical properties are often associated with diseased states, and thus, may provide critical information for early disease detection [1]. Elastography is an imaging modality that can map the local mechanical properties of tissues by measuring tissue deformation that is typically induced by an external excitation. A common type of dynamic elastography reconstructs biomechanical parameters by analyzing properties of a propagating elastic wave. For example, the velocity of the wave can be translated to Young's modulus, and this principle has been widely used in many elastographic modalities, such as ultrasound elastography [2] and magnetic resonant elastography [3]. However, the spatial resolution of

these imaging techniques may restrict their application on small and thin samples [4]. Moreover, these techniques require large amplitude deformations in tissues to achieve sufficient displacement SNR, which may not be feasible in delicate soft tissues.

Optical coherence tomography (OCT) [5] based elastography, termed optical coherence elastography (OCE) [6], is a rapidly emerging technique that can quantify the local biomechanical properties of tissues with micrometer-scale spatial resolution [7]. We have previously reported a non-contact elastic wave imaging optical coherence elastography (EWI-OCE) technique [4], which utilizes point-by-point scanning and allows for two and three dimensional visualization of the low amplitude elastic wave propagation in tissue [8]. This technique has been successfully applied to assess the biomechanical properties of nephritic kidneys [9], cardiac muscle [10], and the cornea [11] among others. The typical EWI-OCE procedure involves acquisition of multiple M-mode images across various spatial positions, usually a line, of the tissue (M-B mode imaging). This in turn requires a mechanical excitation for each OCE measurement position. In this case, the sampling rate of the elastic wave is the A-line rate of the OCT system. Although this method has proven useful for research purposes, long acquisition times of over tens of seconds make this approach impractical for clinical use due to motion artifacts, repeated excitations, and frequently exceeding laser safety exposure limits. Moreover, the large data size (several gigabytes) generated by point-by-point scanning increases the computational cost and makes real-time elastography a challenge. In order to reduce the acquisition time for elastic wave imaging, our group has previously proposed a noncontact phase-sensitive OCE technique at ~ 1.5 million A-lines per second, where successive B-scans (B-M mode) were acquired with a temporal resolution of ~ 7.3 kHz, reducing the total acquisition time to milliseconds and adhering to laser safety limits [12]. Only a single air-pulse was required for one elasticity measurement with this technique. In this case, the sampling rate of the elastic wave is based on the B-scan frame rate. However, there was an intrinsic trade-off between the temporal and transverse spatial resolutions, which constrained the dynamic range of the elasticity measurements. Nahas et al. proposed a full-field OCT system free of transverse mechanical scanning to monitor acoustically generated Scholte wave propagation on the surface of an *ex vivo* rat brain [13]. However, the limited field of view of a few hundred microns and the slow readout time of the two-dimensional camera limited the maximum detectable elastic wave speed. Fourier domain line-field OCT is a high speed imaging modality that provides two-dimensional cross-sectional maps without mechanical scanning [14,15]. However, demonstrated frame rates of a few kilohertz restrict imaging of rapid dynamic motion such as an elastic wave in stiff samples.

Digital holographic imaging is a rapid and noninvasive technique that provide high-precision quantitative phase images [16]. Oldenburg et al., pioneered the use of holographic elastography by monitoring surface acoustic waves and reconstructing sample stiffness from spectral analysis of the wave [17, 18]. This method required a single frame for surface wave reconstruction. Although that technique was capable of quantifying the depth-wise elasticity in tissues, it required prior knowledge of the surface wave frequency and was restricted to wave displacements within $-\pi/2$ to $\pi/2$. These limitation may not be suitable for air-pulse based applications [11, 19], since the displacement amplitude and frequency cannot be known beforehand. In addition, the acquisition frame rate may not be sufficient to capture the air-pulse induced elastic wave, which attenuates within a few millimeters [20]. Previously, Massatsch et al. developed low-coherence gating digital holography and successfully imaged in-depth structure of the porcine cornea and iris [21]. However, this technique was not further evaluated for elastography applications.

In this study, we propose a noncontact single shot elastography using line field low coherent holography (LF-LCH) system to assess the biomechanical properties of tissues. The surface wave propagation induced by a single air-pulse on homogenous and heterogeneous tissue-mimicking phantoms and chicken breast *ex vivo* was successfully imaged by the

system. This method provided a temporal resolution of $62.5 \mu\text{s}$ due to the use of one-dimensional imaging optics and detection, resulting in the ability to acquire a complete spatio-temporal elastogram in less than 20 milliseconds. In addition, each spatio-temporal map needed for a quantitative elasticity assessment was only a few megabytes. The elastic wave velocity detected from the tissue mimicking phantoms and chicken breast samples was translated to Young's modulus by the surface wave equation [19], and the stiffness was compared to the results obtained by uniaxial mechanical testing on the same samples. To further demonstrate the applicability of LF-LCH for elastographic applications, the mechanical anisotropy of chicken breast was assessed by imaging the elastic wave propagation at selected angles relative to the muscle fiber orientation. The LF-LCH line scan rate was 16 kHz, which is among the highest speeds demonstrated for lateral imaging of elastic/surface wave propagation in optical elastography methods.

2. Methods and materials

2.1 Tissue mimicking phantoms and biological samples

To demonstrate the feasibility of LF-LCH, tissue mimicking agar phantoms of various concentrations (1%, 1.5%, and 2% w/w, $N = 4$ for each concentration) were used to validate the proposed technique. Three transversely heterogeneous phantoms, which were composed of 1% and 2% agar concentration components, were created to test the system sensitivity to spatial variations in stiffness. The boundary between the agar concentrations was aligned orthogonally to line beam. LF-LCH was then tested on *ex vivo* chicken breast samples ($N = 3$). Uniaxial mechanical compressional testing (Model 5943, Instron Corp.) was performed on the homogenous phantoms and chicken breast samples immediately after the optical measurements. The chicken breast sample was mounted on a rotational stage to measure the elastic anisotropy. Prior to the experiment, the muscle fiber was aligned parallel to the illumination light beam. Measurements were taken at 0, 45, and 90 degrees ($N = 4$, for each group) by rotating the sample.

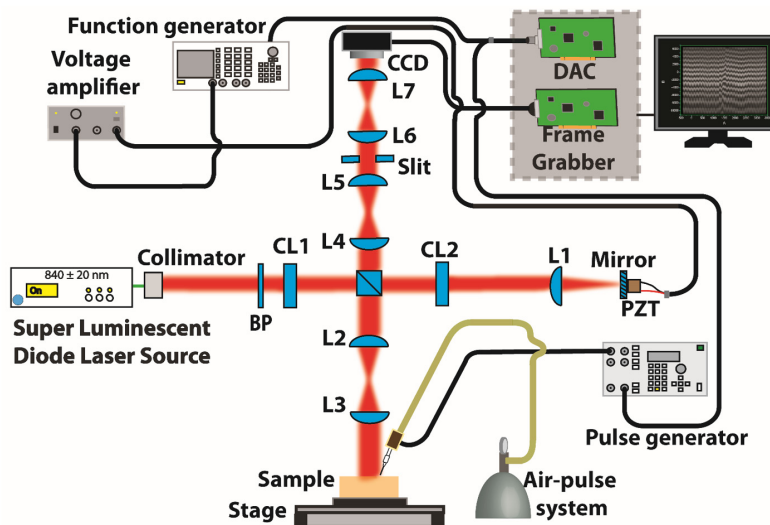


Fig. 1. Schematic setup of line-field LCH system (top view). CL: cylindrical lens. L1-L7: plano-convex lens. DAC: digital to analog converter. PZT: piezo-electric transducer. BP: band pass filter

2.2 LF-LCH system

A schematic of the LF-LCH system is shown in Fig. 1. Low coherence light from an $840 \pm 20 \text{ nm}$ superluminescent diode (SLD) (Broadlighter T-870-HP, SuperLum Diodes, Ltd.) was

expanded to a 4 mm diameter beam using a fiber collimation package (F810APC-842, Thorlabs, Inc.) and directed to a non-polarizing 50:50 beam splitter cube. The output power of the SLD was 2.5 mW and illuminated a line-focused beam of 0.185 mW on the sample due to the use of a 10 nm band pass filter to increase the coherence length of the light. The light was split into the sample and reference arms of the interferometer. A 100 mm focal length cylindrical lens (CL1) was placed in the beam path prior to the beam splitter to generate a line focus. In the sample arm, the line focus was relayed at 1X magnification by a pair of 100 mm focal length lenses (L2, L3) to the sample. The imaged sample was placed in the focal plane of L3. In the reference arm, a matching 100 mm focal length cylindrical lens (CL2) compensated for astigmatism generated by CL1. The reference beam was focused to the surface of a small mirror using an 80 mm focal length achromatic lens (L1). The reference mirror was glued to an open-loop piezoelectric transducer (PA4DGW, Thorlabs, Inc.) which was used to perform Carré four-phase shifting to obtain the phase information [22]. Light reflected from the reference mirror was recombined with the back-scattered light collected from the sample in the beam splitter cube. A relay telescope consisting of two 75 mm focal length lenses (L4, L5) relayed the line focus to a secondary image plane where a horizontal slit was inserted into the beam path to eliminate stray light. The image was relayed onto the active area of a line scan camera with a pixel size of $10\ \mu\text{m}$ by $10\ \mu\text{m}$ (spL4096-140km, Basler, Inc.) by another 4F telescope consisting of two 75 mm focal length lenses (L6, L7). The line focus created at the camera image plane was $\sim 20\ \mu\text{m}$ (FWHM of the point spread function) in height and 4 mm wide, illuminating 450 pixels on the CCD with a pixel resolution of $8.9\ \mu\text{m}$. The system sensitivity was 54 dB measured with an exposure time of $6.5\ \mu\text{s}$ (the sensitivity drop due to difference in focus size and pixel size was $\sim 12\%$). The air-pulse delivery system was synchronized with the frame trigger, and the applied pressure on the sample surface was less than 5 Pa. The details of the air-pulse system were reported in our previous work [23]. The PZT in the reference arm was driven by an 8 kHz symmetric ramp signal and 8 frames were captured for each half cycle of the ramp. The frame rate of the line scan camera was 128 kHz, and the camera was synchronized with the PZT. The elastic wave propagation across the sample surface was captured in the spatio-temporal map with a temporal resolution of $62.5\ \mu\text{s}$ by utilizing both forward and backward scans of the PZT modulation.

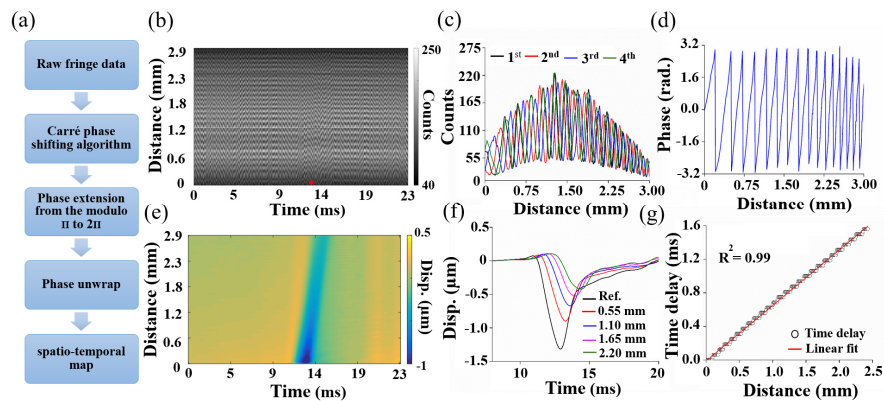


Fig. 2. (a) Phase retrieval workflow. Examples in (b-g) are from a 1% tissue mimicking agar phantom. The red point represents the location of air-pulse excitation. (b) Raw spatio-temporal interferogram (c) Raw fringes with four phase shifts. (d) Wrapped phase across the line scan prior to the air-pulse excitation. (e) The spatio-temporal map after background tilt removal from 23 ms to 47 ms in (b). (f) Selected temporal displacement profiles at a reference position near the wave excitation shown (a) and 0.55 mm, 1.1 mm, 1.65 mm, and 2.2 mm away from the reference location. (g) Linear fitting of selected elastic wave propagation delays obtained by cross-correlation analysis to the corresponding distances of 2.5 mm.

2.3 Phase retrieval procedure

Detailed phase retrieval and post processing procedures are presented in Fig. 2. Examples in Fig. 2(b) to 2(g) are from a tissue mimicking agar phantom made of 1% agar (w/w). The Carré phase shifting technique was selected for phase retrieval as it eliminates the need for PZT phase calibration [22]. The raw spatio-temporal map presented in Fig. 2(b), and Fig. 2(c) shows typical fringes of four phase shifts by the movement of PZT. The fringe modulation in Fig. 2(c) was introduced by a relative tilt between the sample and reference arms. The wrapped phase, as illustrated in Fig. 2(d), was first unwrapped spatially and then temporally without using additional filters. The unwanted phase information out of the focal plane was eliminated due to the coherence gate. The phase unwrapping processes were performed on the forward and backwards PZT scans individually before being combined. Consequently, hysteresis from the PZT resulted in high spatial frequency artifacts in the combined spatio-temporal phase map, which were removed by a 2D 8x8 pixel median filter. The sloped phase background due to the tilt of the reference mirror was removed when quantifying the elastic wave group velocity. The tilt-free spatio-temporal map along the line beam in Fig. 2(b) is presented in Fig. 2(e), where the yellow and blue colors represent the upward and downward displacements, respectively. In addition to the wave propagation, the amplitude attenuation can clearly be seen. To assess the system performance, we characterized the system with the same tissue-mimicking phantom. Prior to the wave arrival as plotted in Fig. 2(e), the phase stability was 12.6 nm over 23 ms as defined by one standard deviation of the temporal phase displacement.

2.4 Quantification of elastic wave group velocity

Five example temporal displacement profiles near the excitation marked by the red point in Fig. 2(b) and 0.55 mm apart are plotted in Fig. 2(f). There is a clear delay as the wave propagates, and the elastic wave group velocity was obtained by cross-correlation analysis of the background subtracted displacement profiles. The subsequent propagation delays were linearly fitted to the respective propagation distances to obtain the elastic wave group velocity [10]. An example of the procedure is shown in Fig. 2(g) using 250 points. The elastic wave group velocity, c_g , was then translated to Young's modulus, E , using the surface wave equation [19],

$$E = \frac{2\rho(1+\nu)^3}{(0.87+1.12\nu)^2} c_g^2 \quad (1)$$

where $\nu = 0.49$ was Poisson's ratio [24]. The density, ρ , was assumed as 1000 kg/m³ for the agar phantoms, and 1120 kg/m³ for chicken breast samples [25].

3. Results

3.1 Homogenous agar results

The Young's moduli of the homogeneous agar phantoms as assessed by LF-LCH and as measured by uniaxial mechanical compression testing are plotted in Fig. 3(a). The Young's modulus of 1% agar phantoms was 7.6 ± 0.5 kPa and 10.4 ± 2.2 kPa as measured by OCE and mechanical testing, respectively. For the 1.5% agar phantoms, the stiffness estimated by OCE was 19.9 ± 1.7 kPa and 27.9 ± 5.5 kPa as measured by mechanical testing. The elasticity of the 2% agar phantoms calculated from OCE measurements was 35.1 ± 2.9 kPa and 37.1 ± 4.7 kPa as measured by mechanical testing. The agreement between the OCE measurements and mechanical testing demonstrate the accuracy of LF-LCH for elasticity assessment.

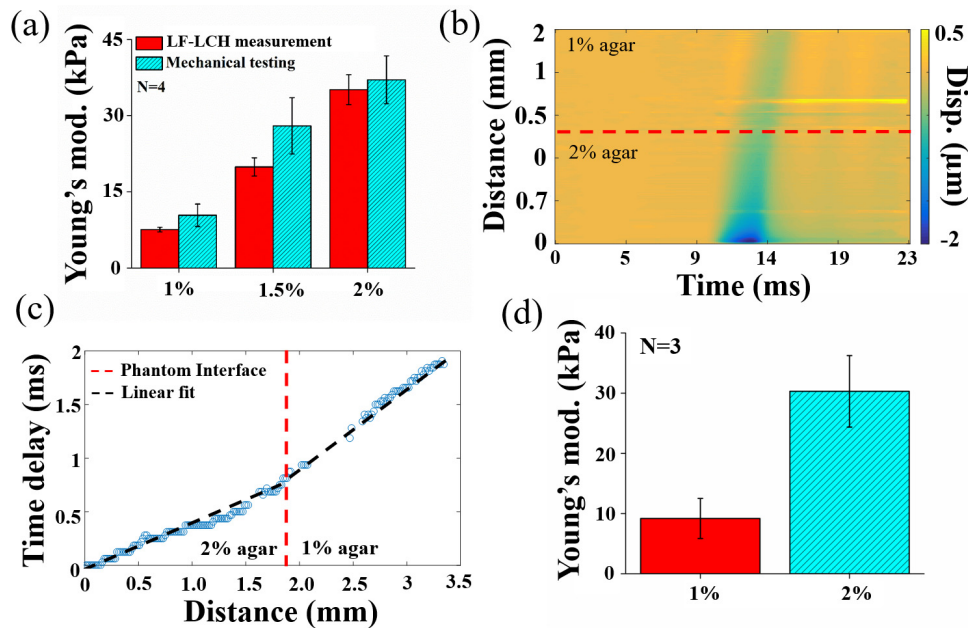


Fig. 3. (a) Young's modulus of homogenous phantoms as assessed by LF-LCH and as measured by uniaxial mechanical compression testing ($N = 4$). (b) Spatio-temporal displacement map of the transversely heterogeneous phantom. (c) The computed propagation time delays of the elastic wave in (b). (d) Young's modulus of 1% and 2% agar components of the heterogeneous phantoms ($N = 3$). The color bar represents the relative displacement values, the red dashed line marks the interface between different agar concentrations, and the error bars represent two standard deviations.

The system performance was further evaluated with transversely heterogeneous agar phantoms composed of 1% and 2% agar. The spatio-temporal map of the elastic wave propagation in a heterogeneous phantom is shown in Fig. 3(b), and wave propagation time delays are plotted in Fig. 3(c). Figure 3(d) depicts the Young's modulus as 30.3 ± 5.9 kPa in 2% agar and $9.17 \text{ kPa} \pm 3.32$ kPa in 1% agar ($N = 3$). These results correlate with the homogenous phantom results, suggesting the LF-LCH system is sensitive to the elasticity changes along the elastic wave propagation path.

3.2 Chicken breast muscle mechanical anisotropy

After these preliminary experiments, *ex vivo* chicken breast elasticity was assessed using the LF-LCH system. The spatio-temporal displacement map shown in Fig. 4(a), and selected temporal displacement profiles plotted in Fig. 4(b) not only show the wave attenuation but also the elastic wave dispersion. The increased width of the elastic wave is well correlated to viscosity by the Voigt model [26]. The elasticity of the chicken breast estimated by OCE was 4.7 ± 1.1 kPa, which is similar to 5.1 ± 1.1 kPa obtained by mechanical compressional testing as plotted in Fig. 4(c).

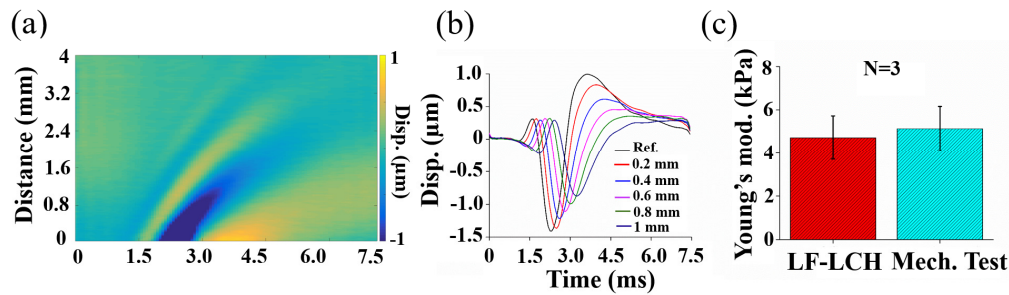


Fig. 4. (a) Spatio-temporal displacement map of the air-pulse induced elastic wave in chicken breast. (b) Selected temporal displacement profiles at the indicated positions. (c) Comparison of Young's modulus results obtained from chicken breast utilizing LF-LCH and uniaxial mechanical compression testing (N = 3).

To explore further applications of the LF-LCH system, the elasticity of a chicken breast sample at various angles oriented with the muscle fibers (0, 45, and 90 degrees relative to the line focused SLD beam) was assessed. In Fig. 5(a), the elastic wave velocity revealed that the stiffness of the chicken breast is the greatest when the fibers are aligned with the line beam and the least when the fibers are aligned orthogonal to the line beam. As a result, the Young's moduli estimated by OCE for 0, 45, and 90 degrees were 49.9 ± 12.5 , 23.6 ± 2.4 , and 14.8 ± 4.0 kPa, respectively, as illustrated in Fig. 5(b). The LF-LCH successfully characterized the mechanical anisotropy of chicken breast.

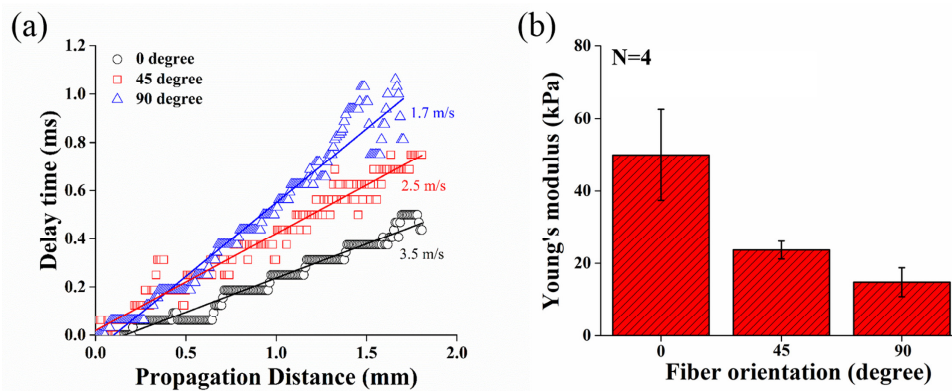


Fig. 5. (a) Selected time delays of the air-pulse induced elastic at various angles relative to the chicken breast muscle fiber orientation. (b) Young's modulus of the chicken at various angles as assessed by LF-LCH.

4. Discussion and conclusions

The proposed system successfully demonstrates a noncontact quantitative optical elastographic assessment with ultra-short acquisition time of a few milliseconds. Considering the time for the tissue to return to its displacement before the air-pulse, the data acquisition time can be further reduced to ~ 6 ms, which is at least a thousand times faster than the previously proposed EWI-OCE technique [4]. However, the Young's modulus as estimated by LF-LCH in Fig. 3(a) was underestimated as compared with mechanical compression testing. These results corroborate with our previous work that showed that the surface wave equation underestimates the stiffness of phantoms as compared to mechanical testing [19]. This may be due to the nonlinear characteristics of the stress-strain curve of the agar phantoms and the assumptions about sample geometry in the surface wave equation. Moreover, spectral analysis can provide the basis for more robust mechanical models such as the Rayleigh-Lamb frequency equation to provide more accurate assessment of viscoelasticity

as compared to the surface wave equation [19]. Nevertheless, the LF-LCH results were in good agreement with uniaxial mechanical compressional testing, demonstrating that the presented method accurately detect the elasticity of homogenous phantoms in a few milliseconds.

The results of the transversely heterogeneous phantom shown in Fig. 3(b) to 3(d) demonstrated that LF-LCH system is sensitive to elasticity changes along the elastic wave propagation path. However, the topographical difference of the phantom surface at the boundary between the 1% and 2% agar components reduced the fringe visibility and generated local phase unwrapping errors appearing as the horizontal strips from 2.2 mm to 2.5 mm in Fig. 3(b). The corresponding detected time delays were filtered out in Fig. 3(c) to increase the accuracy of the velocity calculation. To correct the phase errors at regions with low fringe visibility, Meneses et al. proposed a local histogram filter algorithm [27]. Integrating this technique to the current LF-LCH post-processing is the next step in improving the robustness of the LF-LCH system and is an avenue of our future work.

Furthermore, due to the relatively large extent of the line focus (4 mm), the surface curvature and roughness can spatially deform the wavefront and cause difficulty in obtaining continuous interference across the imaged surface. In this case, if the degree of wavefront deformation exceeds the coherence length, interference will not occur at the corresponding spatial pixels. Gating has been successfully used for supersonic shear imaging applications [28, 29] and is a promising technique for *in vivo* elastographic application with the presented system. Also, we utilized a 10 nm bandpass filter to increase the coherence length for maintaining interference across the line beam. However, this had the drawback of drastically reducing the illumination power, which limited the ability to perform tomographic imaging. In addition, it is inevitable that the living subject may move out of the coherence gate, due to, e.g., cardiac motion. To resolve this problem, ECG gating synchronized with ultrasound imaging system at a frame rate of 8 kHz has been used successfully for *in vivo* supersonic shear wave imaging of cardiac tissues [28]. Thus, incorporating a light source with higher power and narrower bandwidth, and developing a temporal gating technique may be important for the future work.

Previously, Massatsch et al. has successfully imaged the structure of porcine cornea and iris using similar low-coherent holographic microscopy setup [21]. This work promises the feasibility of addressing cornea curvature problem by imaging a small *en face* field-of-view of 240 μm x 250 μm with coherence length of 24 μm , continuous interference. As a result, they successfully imaged the full cornea thickness of ~ 1 mm. However, it may be challenging to capture multiple frames of the elastic wave propagation within such a small-field-of-view.

Characterizing the system dynamic range of elasticity assessment is important to accurately perform quantitative elastography with the LF-LCH system. To reliably quantify the propagating elastic wave speed, at least 5 temporally delayed pixels were needed for accurate cross-correlation across the 3 mm line within an optimized acquisition window of 6 ms. As a result, the LF-LCH system can provide a detectable Young's modulus of 0.82 kPa to 302 kPa based on the Eq. (1), which is sufficient for assessing the elasticity properties of a vast majority of soft tissues. As compared with previous 1.5 MHz OCE technique (B-M mode) [12], the LF-LCH setup not only has a greater dynamic range of elasticity assessment, but also a higher spatial pixel resolution of 8.9 μm , which is 4.5 times higher than the 1.5 MHz OCE technique.

The anisotropy results in Fig. 5 are consistent with previous work by Gennisson et al. [30] and demonstrate the feasibility of LF-LCH to detect the mechanical anisotropy of muscle. More importantly, due to a single shot excitation, an elasticity assessment only required one frame that was only a few megabytes, which dramatically reduced the data processing time and storage space as compared with point scan techniques. Thus, the results not only demonstrate the feasibility of LF-LCH for biological applications, but also suggest the

potential for performing real-time elastic wave imaging on account of dramatically reduced computational cost and data storage.

In addition to the analysis of elastic wave group velocity, the depth-resolved elasticity changes can be retrieved from the surface wave utilizing spectral analysis [31]. However, insufficient lateral scanning resolution may cause phase unwrapping errors in space, and the long acquisition time may introduce phase noise caused by environmental or sample motion. To this end, the LF-LCH system may reduce the phase noise due to high transverse spatial resolution and ultra-fast acquisition speed. As compared with the previously reported noncontact true kilohertz frame-rate OCE system [12], LF-LCH maintains higher transverse spatial resolution of 8.9 μm as determined by the CCD pixel dimensions and thus, may provide more precise and accurate depth-wise characterization of biomechanical properties.

However, the system phase stability and line acquisition rate were constrained by the PZT. The mechanical hysteresis generated high spatial frequency noise, and the nonlinear movement in response to applied voltages resulted in periodic phase errors and reduced phase stability [32]. A closed-loop PZT with more linear and hysteresis-free movement is necessary to overcome phase aberrations caused by the mechanical motion. On the other hand, spatial phase shifting can obtain phase information without PZT modulation [33], and utilizing this technique is another option for increasing the line scan rate to ≥ 200 kHz and phase stability. Both of these techniques have different advantages and disadvantages [34] and are avenues of our future work.

To address laser safety, we consider the maximum permissible exposure (MPE) for light incident on the eye under Maxwellian illumination conditions (i.e. light intentionally focused on the anterior segment of the eye). Under these conditions we must consider the safety limits for both the retina and cornea. We used an illumination power of 0.185 mW over $0.8 \times 10^{-3} \text{ cm}^2$ with a total exposure time $t = 23$ ms. The corresponding intensity was 231.25 mW/cm². The calculations of maximum permissible radiant power (MP Φ) entering the natural or dilated pupil is based on the American National Standard Institute (ANSI) Z136.1-2000 standard [35]:

$$MP\Phi = 6.96 \times 10^{-4} * C_T * C_E * t^{-0.25} [W] \quad (2)$$

where C_T is a wavelength dependent factor (1.9) and C_E is a correction factor depending on source types. According to the laser safety calculations reported by Delori et al [35], the C_E parameter of small point source was assumed to be 1 and resulted in an MP Φ of 3.4 mW. However, in the case of the rectangular illumination used by LF-LCH, the correction factor C_E was:

$$C_E = \frac{8\alpha_L\alpha_w}{\pi\alpha_{\min(\alpha_L+\alpha_w)}} \quad (3)$$

where the subtended angles in the length axis α_L , the width axis α_w , and α_{\min} were 40 mrad, 1.5 mrad, and 1.5 mrad, respectively. Based on Eqs. (2) and (3), the MP Φ for the line-field illumination is relaxed to 8.35 mW with the C_E factor of 2.45. The maximum permissible exposure (MPE) limits for the cornea (42.3 W/cm²) and skin (35.4 W/cm²) were also not exceeded according to Eqs. (4) and (5):

$$MPE_{\text{cornea}} = 2.5t^{-0.75} [\text{W/cm}^2] \quad (4)$$

$$MPE_{\text{skin}} = 1.1C_T t^{-0.75} [\text{W/cm}^2] \quad (5)$$

where t is the exposure time (23ms), and C_T is a wavelength dependent factor (1.9). Consequently, this technique is safe for *in vivo* use on the cornea and skin due to its rapid acquisition speed and adherence to laser safety limits.

In summary, we have successfully demonstrated a novel noncontact single shot LF-LCH technique with high temporal resolution of 62.5 μ s. This system successfully imaged the propagation of an air-pulse induced elastic wave in homogenous and transversely heterogeneous tissue mimicking phantoms. Furthermore, the mechanical anisotropy of *ex vivo* chicken breast was assessed. The LF-LCH system had a 16 kHz line scan rate with a spatial pixel resolution of 8.9 μ m. The rapid acquisition suggests the potential of this technique to overcome motion artifacts such as heartbeats or ocular microsaccades. Future work will involve phase velocity analysis, automated instrumentation, and developing a more robust phase unwrapping algorithm for accurately retrieving the phase in the areas with low fringe visibility. With the single shot acquisition, safety limit adherence, reduced data storage, simple optical instrumentation, and relatively cost-effective setup, the proposed results show potential for clinical assessment of tissue biomechanical properties utilizing LF-LCH.

Funding

This work was funded in part by the grants from National Institutes of Health (NIH) (1R01EY022362, 2R01EY022362, 1R01HL120140, and U54HG006348).

Acknowledgments

We are grateful for the experimental assistance from Ms. Ericka Lafon and Ms. Raksha Raghunathan.